Shape principal component analysis as a targetless photogrammetric technique for condition monitoring of rotating machines

Benjamin Gwashavanhu, P. Stephan Heyns* and Abrie J. Oberholster

Centre for Asset Integrity Management, Department of Mechanical and Aeronautical Engineering, University of Pretoria, Pretoria, South Africa

*Corresponding author.

Centre for Asset Integrity Management, Department of Mechanical and Aeronautical Engineering, University of Pretoria, Pretoria, South Africa. Email: stephan.heyns@up.ac.za

Highlights

- Applicability of shape principal component analysis as a dynamic analysis tool.
- Condition monitoring of a rotating machine using approach successfully performed.
- A multi-dimensional targetless approach successfully compared to uniaxial sensors.

Abstract

Rotating machines are widely used in engineering for applications which include power generation and machine propulsion systems. These machines have to be accurately monitored and maintained to avoid system failures. Vibration analysis, which involves the use of contact and non-contact measurement techniques to capture vibrational data indicative of the condition of a machine, is normally used for this purpose. 3D Point Tracking (3DPT) and Digital Image Correlation (DIC) constitute photogrammetric-based optical non-contact measurement techniques that have proven to be efficient for the vibration analysis of rotating machinery. In addition to complex image processing software and tracking algorithms, these two approaches typically require surface preparation in the form of markers and speckle patterns. These requirements limit the applicability of photogrammetry as a condition monitoring tool, especially when it comes to industrial environments. This paper proposes 2D shape analysis for target-less non-contact measurement in condition monitoring of rotating machines. Through comparison to measurements captured using conventional proximity probes on an experimental test setup, it is also illustrated how different dynamic characteristics of a rotating system can be distinguished using this measurement approach.

Keywords: Photogrammetry; Shape principal component analysis; Condition monitoring; Rotating machinery

1. Introduction

Various maintenance strategies are implemented to avoid or minimize failure of rotating machinery. These can either be corrective or preventive maintenance strategies. Preventive based approaches offer the advantage of ensuring that parts are replaced before a system fails, which in most cases would mean high cost of repair and machine downtime losses. Vibration based condition monitoring is commonly employed in developing reliable preventive maintenance strategies. The vibration signals associated with rotating machinery can be analysed to understand the dynamic characteristics of the machine. These characteristics vary for different machine health states and thus can be monitored to track the condition of a machine.

To monitor a rotating machine for bearing, shaft-rub, misalignment or rotor imbalance faults, one would require two proximity probes at each bearing for monitoring the shaft orbital position and/or two uniaxial accelerometers for structural vibration measurement. Typically, a tachometer is also required for monitoring the rotational speed. These transducers have to be attached at different bearings on the machine whilst it is not running. Accurate diagnosis of the machine is then achieved by comparing measurements captured by the different sensors using approaches such as signal phase analysis. However, contact transducers may interfere with the operation and response of the machine under investigation, whereas eddy current probes require machining for installation. Alternatively, non-contact optical measurement techniques such as Laser Doppler Vibrometry (LDV) and photogrammetry can be employed. These techniques do however require a clear line of sight of the structure under investigation. This is also a requirement in the condition monitoring approach proposed here.

For photogrammetry, 3D Point Tracking (3DPT) and Digital Image Correlation (DIC) have been successfully used for condition monitoring purposes. Using two or more high-speed cameras, a sequence of stereo images can be captured whilst a structure is vibrating. 3DPT and DIC have been successfully employed by a number of researchers [1], [2], [3], [4], [5], [6], [7], [8], [9] and the techniques have proven to be robust for both data capturing and condition monitoring purposes. The accuracy of 3DPT as a measurement technique has been investigated for both static and rotating applications [10], [11]. For rotating applications, it has been shown that 3DPT is reliable enough to capture online out-of-plane blade vibrations that differ from Tracking Laser Doppler Vibrometry (TLDV) measurements by not more than 2.5% and 0.076% in terms vibration magnitudes and frequencies respectively [10].

The disadvantage of 3DPT and DIC is that both these approaches typically require surface preparation such as surface treatment to change the reflective properties of surfaces, or the application of markers, spray painting or etching. As an alternative approach not requiring surface preparation, shape analysis is considered in this paper. Shape analysis is typically used for shape recognition and matching purposes. For instance handwritten digits by different people can appear similar to an observer, but have very different pixel arrangements. If these digits are to be captured using an automated system, some form of shape recognition and matching will have to be applied. If the concept of shape analysis can be applied to a dynamic situation whereby changes of shapes on a structure are analysed,

monitored and compared, then the technique could be a useful tool for online condition monitoring of rotating machinery.

When considering shape analysis applications, Kazmi et al. [12] outlined features that constitute effective shape descriptors. These include discriminative accuracy, transformation invariance, robustness against model degeneracies, and performance and memory efficiency. Simple descriptors that one can monitor include the area, aspect ratio, normalized central moments and perimeter of a shape. These geometric features are however not efficient as shape descriptors, and do not contain much information when compared to shape features [13]. More sophisticated shape descriptors such as Curvature Scale Space (CSS), Wavelet Descriptors (WD) and Fourier Descriptors (FDs) have therefore been proposed [12]. These tend to be more sensitive to various shape changes and can be categorised as contour based, region based or hybrid descriptors. Contour based descriptors focus on feature extraction from shape contours, whilst region based descriptors consider the whole shape [12]. Zhang et al. [14] present a clear classification of these different shape representation and description techniques.

The feasibility of rotating machinery condition monitoring through shape analysis is investigated in this paper, with efforts being focused on developing a photogrammetric measurement technique that is robust and applicable to a wider range of situations. The use of a shape analysis based approach promises potential benefits in terms of limiting the number of transducers needed per bearing housing to accurately diagnose a machine.

Contour based analysis involves investigation of 2D shape variation of images captured in a non-contact manner using a single camera. Thus in addition to the acquiring translational vibrations similar to those captured by contact transducers at a specific shaft location, a 2D shape analysis might also allow acquisition of information representative of the variation in the shaft Operational Deflection Shape (ODS). This is expected owing to the fact that the variation of an enclosed shape at a bearing housing is directly influenced by deflection shape resulting from the rotating shaft whirling motion. Another important advantage of using shape analysis is that the approach can be applied to a running machine, without the need for system shutdown.

2. Contour based shape analysis

Contour based Fourier Descriptors (FDs) are considered in this study. In addition to being relatively easy to compute, Kazmi et al. [12] indicate that FDs are also insensitive to noise and can capture both local and global features. These can be determined for a closed contour describing a shape of interest. The closed contour can be obtained by the use of Freeman's chain code [15]. As described by Jusoh and Zain [16], a chain code represents a boundary of interest based on either 4-connectivity or 8-connectivity of segments. For this investigation, the 8-connectivity chain code forms the shape signature that represents the boundary pixels of an object with a 1D function. It is created by tracing the mid-points of the boundary pixels in a counter clock-wise direction. For the 8-directional chain-code, each integer in the code will be a value between 0 and 7 depending on its orientation relative to the previous pixel.

As stipulated by Kuhl and Giardina [17], a Fourier series representation can be used when extracting the shape descriptors, since the code repeats itself on successive traversals of a contour. The Fourier coefficients of the chain-coded contour form the FDs for that particular shape. For a closed chain coded contour projected on the xy-plane, the elliptical Fourier series approximating the contour can be defined using the equations below [13].

$$x_n(p) = A_0 + \sum_{n=1}^{N} a_n \cos\left(\frac{2n\pi p}{P}\right) + b_n \sin\left(\frac{2n\pi p}{P}\right) \quad (1)$$

$$y_n(p) = C_0 + \sum_{n=1}^{N} c_n \cos\left(\frac{2n\pi p}{P}\right) + d_n \sin\left(\frac{2n\pi p}{P}\right) \quad (2)$$

In the above expressions, the geometric step to move from one pixel to the next is given by

. P is the geometrical period of the chain code, andgives the number of Fourier harmonics considered. Detailed descriptions on the derivations of these coefficients can be found in [13], [17]. The Fourier power of a harmonic, which indicates the amount of shape information described by that particular harmonic [13], can be used to estimate the number of harmonics required.

$$Fourier\ \ power = \frac{\sum_{n=1}^{N} (a_n^2 + b_n^2 + c_n^2 + d_n^2)}{2} \quad (3)$$

The average cumulative Fourier power percentage increases with the number of considered Fourier harmonics. The number of harmonics required for the truncated Fourier coefficients can thus be determined based on the preferred average cumulative power percentage. A high average cumulative power percentage ensures that the local shape features are captured more accurately.

Once the normalized coefficients of the truncated Fourier representation of the chain-code have been obtained, a standard Principal Component Analysis (PCA) on the multivariate vector can be conducted to evaluate the different shape descriptors. PCA is a data reduction procedure that projects possibly correlated data into a reduced space comprising of linearly uncorrelated variables called Principal Components (PCs). In this case, it is not the data reduction that is of importance when performing 2D shape analysis, but rather the uncorrelated nature of the computed PCs. The uncorrelated PCs each represent a unique shape variation which can be monitored separately to give in-depth insight on how the overall shape is changing in a dynamic situation. Each PC represents an independent shape feature which allow a quantitative analysis of the shape to be conducted by use of PC scores as the ordinary quantitative characters [13]. The PCs each represent a specific unique shape variation independent of variations associated with the other PCs. This is illustrated in Section 2.2 of this paper. In general data reduction applications only the first few PCs are considered since the significance of the PCs decreases from the first one going on to the higher number PCs. For 2D shape analysis however, the first PCs tend to capture the global shape features, whilst the last PCs capture the local shape features.

When performing PCA on multivariate vectors, the number of components into which the signal is decomposed to, depends on the dimension of the multivariate vector. The number of PCs is always equal to the number of variables in the multivariate vector. Starting off with

a multivariate vector of four variables (normalised Fourier coefficients) a4 × 4 covariance matrix can be calculated from which four eigenvectors (*V*) are then determined. Each column of the 4 × 4 eigenvector matrix represents a single PC, whose scores are given by the corresponding row of matrix B_t^{new} calculated using Eq. (4).

$$B_t^{new} = V^T B_t \tag{4}$$

In Eq. (4), B_t is the original correlated multivariate vector of the Fourier coefficients. The Euclidean norms of each column of the eigenvector determined for a particular shape in an image can then be considered as the four PC values representative of that shape.

The described analysis implemented on each of the captured images of a running machine can be summarised using a flow diagram given in Fig. 1.

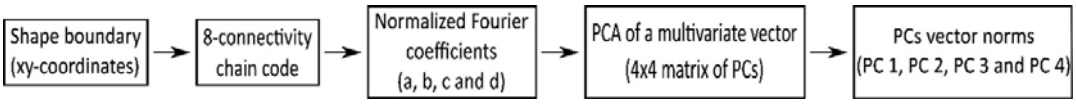

Fig. 1. Image processing flow chart.

For a time sequence of captured images, variations of the four parameters from one image to the next can then be analysed in the frequency domain to extract information descriptive of the manner in which a machine is operating.

3. Typical shape extraction procedure

An image of the shaft location relative to a bearing housing can be captured for a simple rotor system based on the Bently Nevada rotor kit shown in Fig. 2(a). The setup consists of a 455 mm long, 9.5 mm diameter steel shaft onto which are mounted two 25 mm thick, 75.5 mm diameter flywheels. The system is driven by a 75 W DC motor through a flexible coupling, and the other end of the shaft is supported by a fluid film journal bearing. The maximum speed of the system is 10,000 rpm, with a maximum ramp rate of about 15,000 rpm/min. A bush bearing supports the system at the driven end of the shaft.

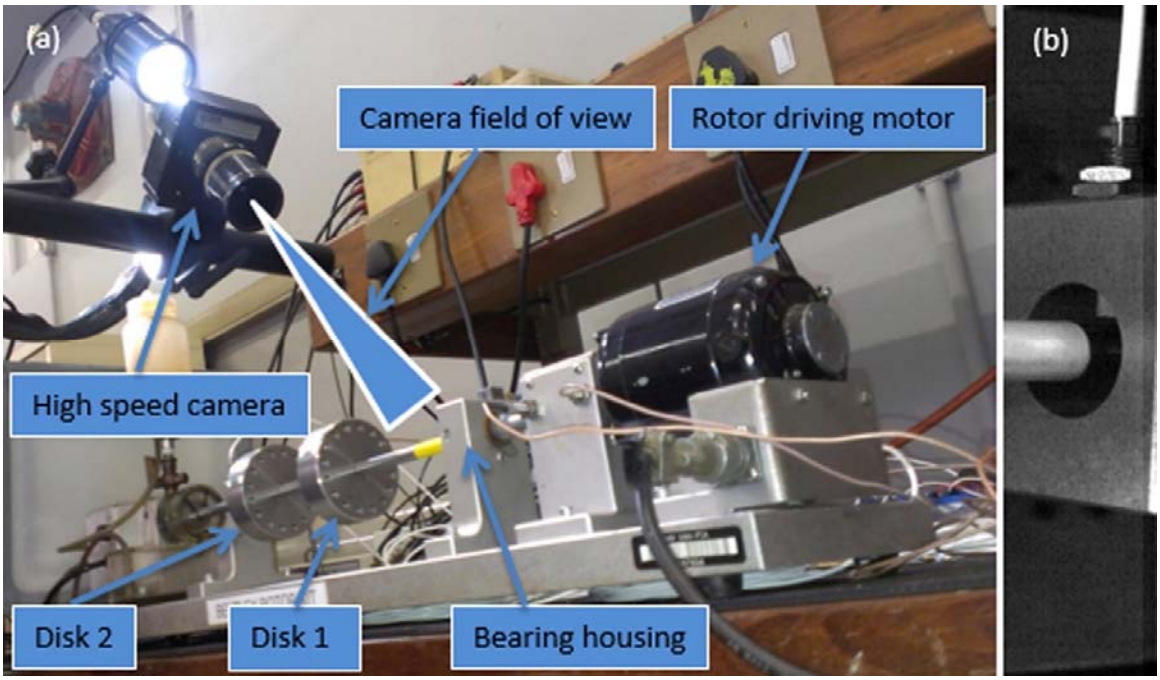

Fig. 2. (a) System setup for a Bently Nevada rotor system, (b) single camera field of view.

Images captured by the camera, similar to the one in Fig. 2(b), can then be processed to extract 2D contours. Fig. 3 shows the captured and processed images from which a contour is obtained. The image processing stages were implemented in LabVIEW using the National Instrument Vision Assistant toolkit.

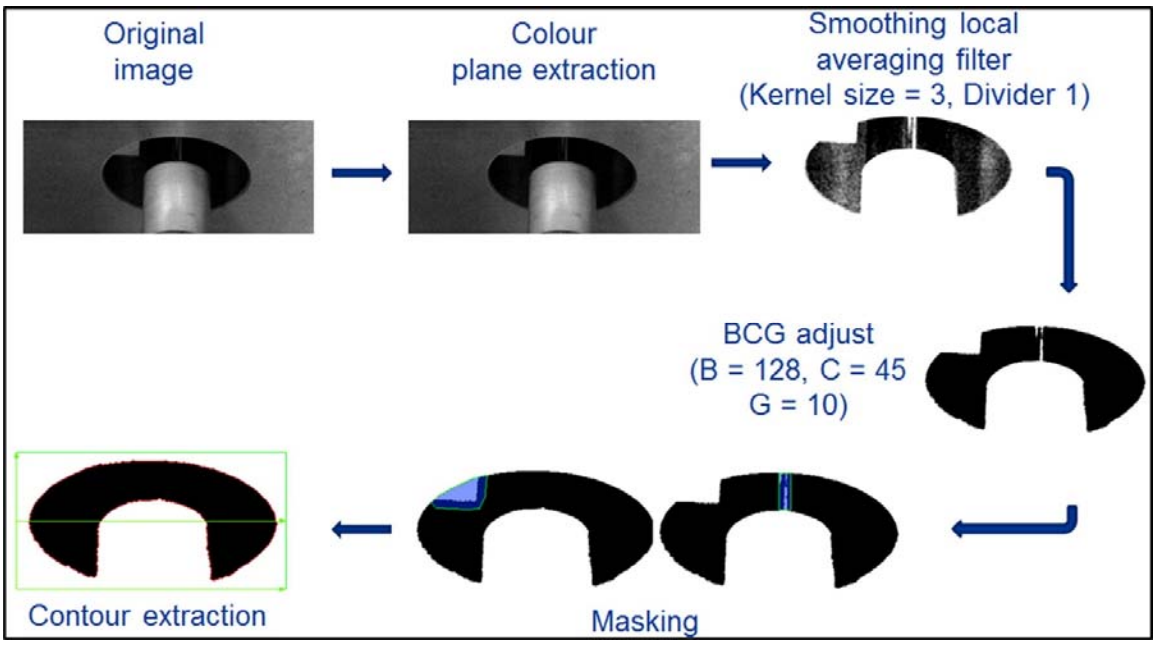

Fig. 3. Contour extraction steps.

Starting with an original image, a colour plane extraction is implemented to obtain a grayscale image to which a smoothing filter is applied to isolate the region enclosed between the shaft and bearing housing. After performing brightness, contrast and gamma corrections to improve the picture luminance, masking of pixels (whose intensities differ significantly from the rest) is performed to allow for the extraction of a smooth continuous contour of the boundary pixels. Pixel masking is performed by drawing polygons enclosing the regions of interest, and then assigning a grayscale value of zero to the covered pixels. It is not a requirement to mask out the probe noticeable on the top left corner of the isolated region between the shaft and bearing housing. For this analysis all that is required is a continuous contour, of which the variation is of more importance than the initial shape form. The image processing presented here understandably depends on the quality of the images captured as determined by the camera resolution and the lighting conditions. After a contour has been extracted, the Fourier coefficients representative of the contour can be extracted and PCA applied to obtain the PCs that can be analysed for each captured image.

The applicability of the approach is not limited to investigations where there exist an enclosed shape between a shaft and a bearing housing. The specific setup adopted here was chosen as it allowed easier verification of measurements using data from proximity probes attached at the bearing housing. As long as a continuous closed boundary of a structure or component changes as a result of the dynamics of the system, then shape variation analysis coupled with shape based PCA can be employed as a condition monitoring tool. This means that the approach can be extended to applications such as turbine blades dynamic analysis. The blade boundaries can be extracted and 3D shape variations resulting from the out-of-plane and torsional vibrations analysed to better understand the blade dynamics or isolate damaged blades based on differences in dynamic behaviour.

4. Analytical based PCA investigation of a 2D shape

A simple numerical investigation of a shape similar to that which can be extracted from an image of the space enclosed between a shaft and a bearing housing was conducted. This was done to better understand how the different PCs affect the form of the shape of interest. The feasibility of condition monitoring of rotating machines using PCA shape analysis was also investigated.

4.1. Effects of different PCs on the form of a 2D shape

To investigate the effect of different PCs on the form of a typical 2D shape, the four PCs of a shape were determined and then their scores scaled one at a time before reconstruction of the original shape. To allow for better visualization of each PC's effect on the shape, different Scaling Factors (SF) were applied to different PCs. Fig. 4 illustrates the results obtained.

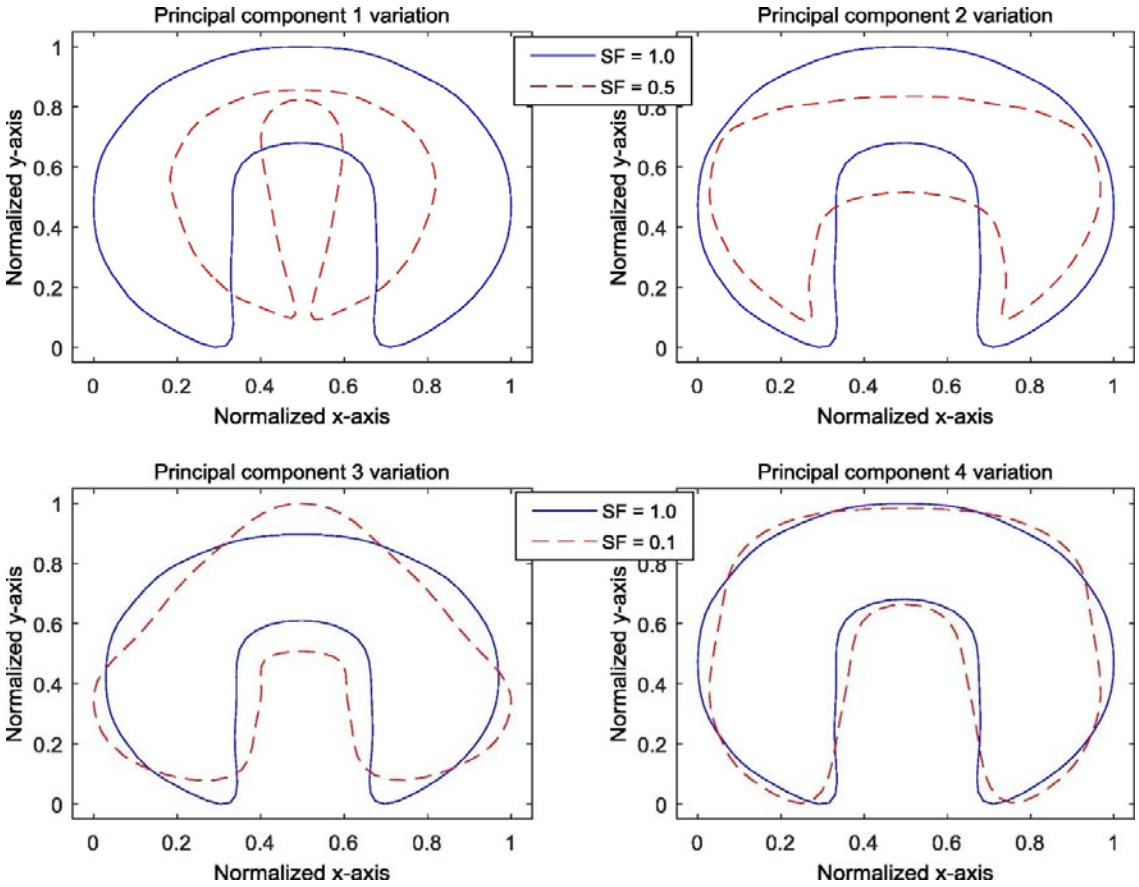

Fig. 4. Effects of principal component variations on the form of the shape. Note the different SFs.

From Fig. 4, the first PC affects the overall size of the shape, without addition of any lobes. The second PC is mostly associated with a shape variation that conserves the distance between the two horizontal vertices whilst the overall shape size changes. The third PC affects the shape skewness, resulting in a three lobe characterized shape. The fourth PC conserves the distance between the horizontal vertices, whilst the vertical vertices move to create a four lobe characteristic shape.

This investigation identifies the effects of the various PCs on the shape. It is evident that each PC has influence on more than a single displacement or rotational degree of freedom. Additionally, the extent to which each PC influences various shape forms differs, as is evident from the different SFs that have to be applied to obtain noticeable shape changes for PC 3 and PC 4. PCs 3 and 4 have a much reduced effect on the shape form as compared to PCs 1 and 2.

Instead of using single axis based transducers were a single parameter is obtained for a single transducer, variations in four PCs caused by various shape changes could be employed for condition monitoring purposes. Extraction of more detailed information about a system is expected in this case since PCs consider 2D shape variations instead of the six degrees of motion of distinct points individually.

4.2. Feasibility of condition monitoring using 2D shape analysis

The applicability of a 2D shape analysis for condition monitoring of a rotating machine is subsequently investigated using an artificially created 2D shape with a form similar to the one indicated in Fig. 4. The outer contour of the shape represents the bearing housing and the inner contour the shaft. The position of the shaft contour is varied using sinusoidal displacements to simulate shaft motion. For the in-plane motion, the virtual shaft can be moved in either a single direction or in both x- and y-directions. By using sine and cosine signals to move the shaft in the x- and y-directions respectively, shaft whirl motion can be simulated. Three different shaft forced motions are simulated. These are forced displacements in the x-direction, y-direction, and a combination of both x- and y-direction. This is conducted to investigate the variation in the PCs of the extracted 2D shape in each case. Fig. 5 below illustrates these imposed shaft displacements.

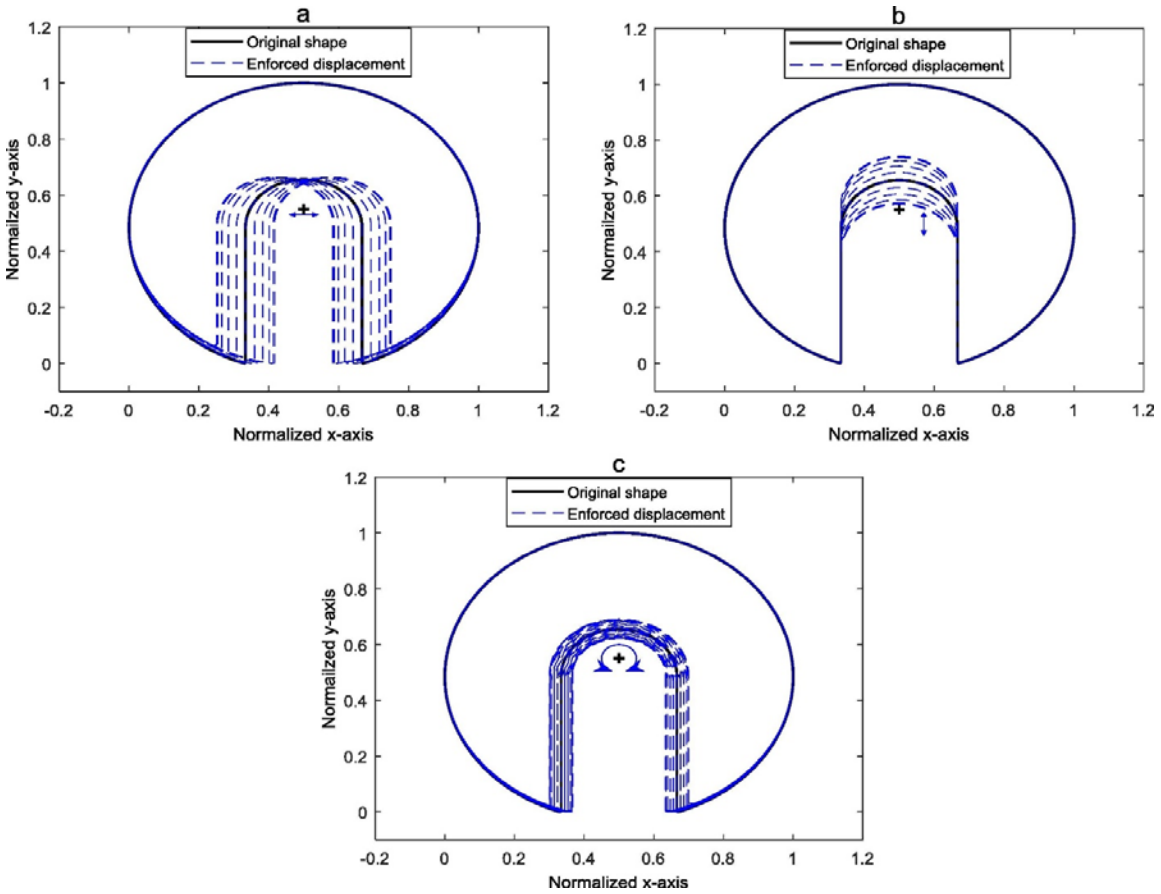

Fig. 5. Forced shaft displacements, (a) horizontal motion, (b) vertical motion and (c) whirling motion.

With forced displacements at a frequency of 20 Hz, the following PC Euclidean norms are obtained in the frequency domain. As can be noted in Fig. 6, all the PCs have peaks at the excitation frequency of 20 Hz, as well as the 2×, 3× and 4× harmonics.

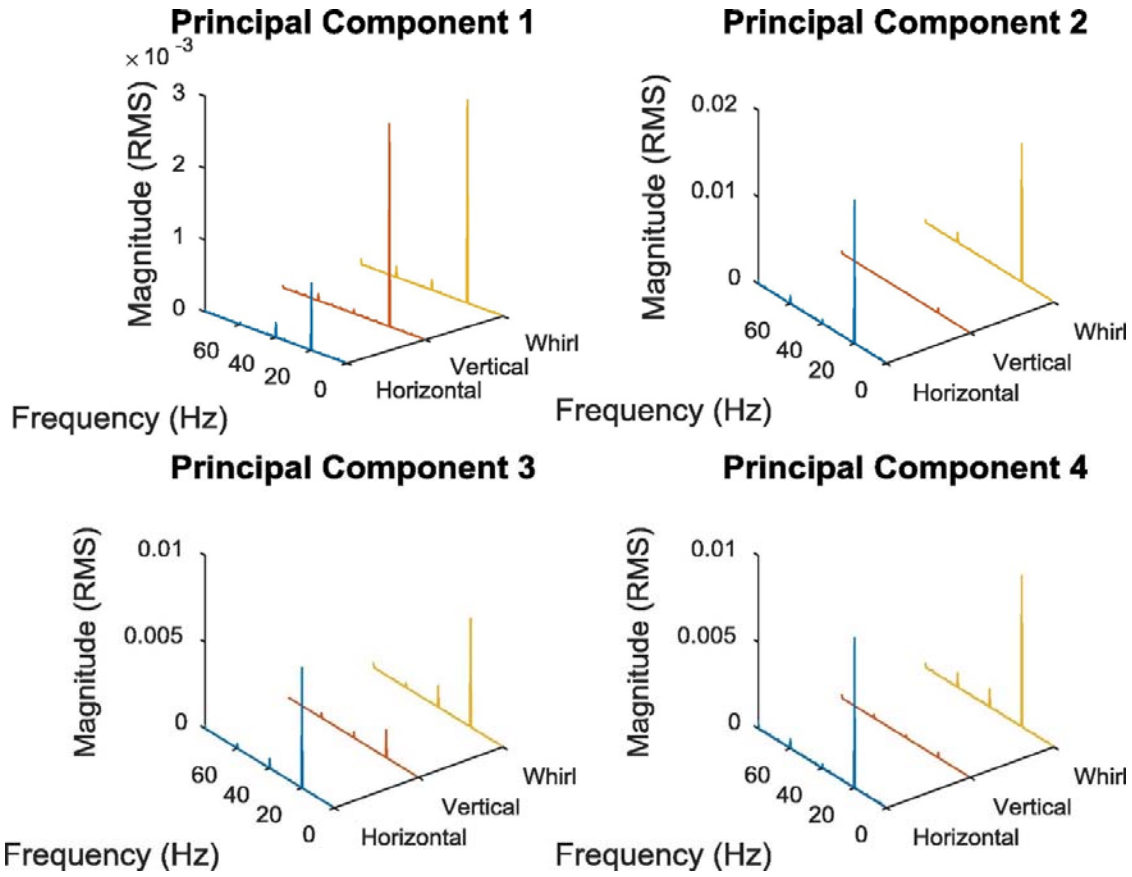

Fig. 6. Principal components system frequency responses.

For PC 1, the vertical and whirl motions have the same magnitudes at the fundamental frequency, with the horizontal motion having the least influence on the PC. It is evident that pure shaft vertical motion has the least influence on the shape's second, third and fourth PCs, whilst the first PC variation indicated in Fig. 6 depicts a shape variation that is more or less similar to what is obtained when a shaft is moving entirely up and down. PCs 2, 3 and 4 have shape variations that do not describe vertical shaft motions.

The harmonics present in Fig. 6 are expected since none of the forced motions correspond identically to the shape variations associated with the PCs illustrated in Fig. 4. In the same way that sine signals are considered to be pure tones from which other periodic signals such as square and saw tooth waves can be created, the shape variations illustrated in Fig. 4 can be considered as pure PCs shape variations. When performing 2D shape analysis in the frequency domain, general shape variations such as shaft whirling motion that deviate from the pure PCs shape variations are approximated by sums of pure PCs variations with frequencies corresponding to the harmonics of fundamental forcing frequency (Fourier analysis application). Owing to the significant differences that can occur between the pure PC shape variations and the forced shaft whirling motions, it is possible that sometimes the harmonics contain more energy than the fundamental frequency, as observed in some of the PC results presented below and in Section 5 of this paper.

As an illustration, forced shape variations given in Fig. 7 are identical to one cycle variations associated with PC 4 (similar to Fig. 4 PC 4 shape). In this case one would expect frequency responses with a single peak at the forcing frequency for PC 4 and different results for the other PCs.

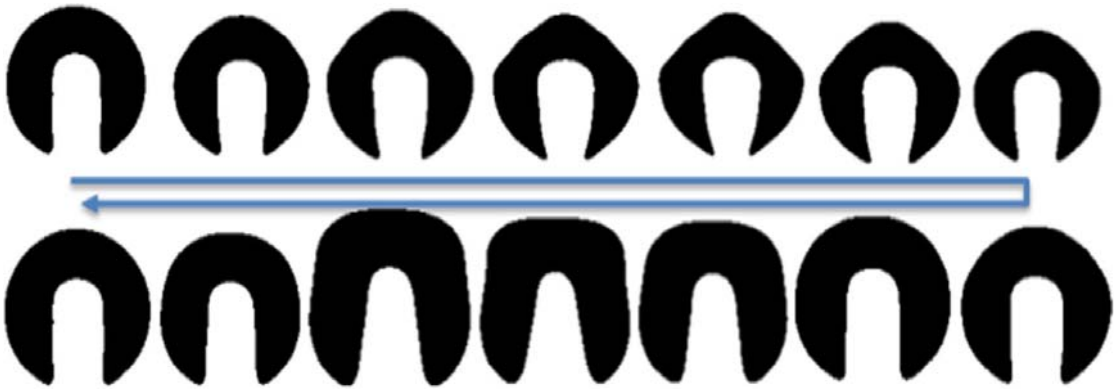

Fig. 7. Typical one cycle forced shape variation associated with a single PC (PC 4 in this case).

Results obtained for forced shape variations identical to each of the four PCs are given in Fig. 8 for forcing frequency of 20 Hz.

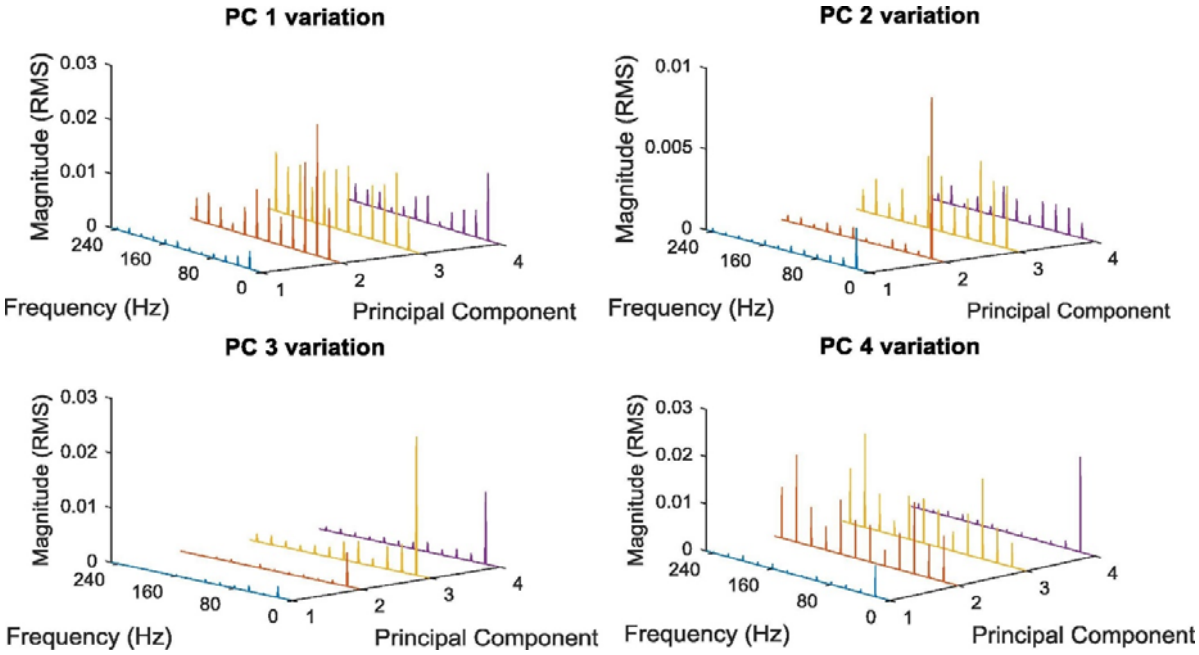

Fig. 8. PC responses to specific forced shape variations.

For forced shape variations associated with different PCs, Fig. 8 shows that the PC of interest tends to show significant peaks at the fundamental frequency, with the rest of the PCs indicating their most dominant peaks at higher harmonics. Peaks at the fundamental frequency of the PC of interest also have higher magnitudes than the remaining PCs, with the exception of PC 1. As mentioned earlier, PC 1 is associated with overall size variation. When forced explicitly, PC 1 variation tends to effect shape changes that influence the other

PCs more. This is a result of cross sensitivity between the PC 1 shape variation and shape variations associated with the other PCs. Considering the behaviour of PC 1 to forced shape variations representative of all the other PCs, it can be observed that PC 1 always has its most significant peak at the fundamental frequency, but with lower magnitudes.

Thus when considering shaft whirling motion, the harmonics observed in PC results do indicate presence of information that is entirely associated with how the forced shape variation differs from the shape variation associated with a particular PC. This information can be used to complement conventional single point sensor measurements. The above investigation shows that Fourier shape descriptors can be used to extract four different parameters in the form of PCs. These evidently vary with various changes in the shape, implying that they can be monitored to characterize dynamics of vibrating structures.

A sensitivity analysis conducted by Gwashavanhu et al. [18] indicated that the positioning of the camera affect the captured PCs. For vertical camera location variation, it was shown that PCs 2 and 3 become more sensitive to shape variations whilst sensitivity generally decreases for PC 4. PC 1 sensitivity increases to a maximum at 50^0 and then decreases. The camera position along the horizontal axis does not influence the sensitivity of the four PCs. It was also shown that a camera frame rate of at least four times the frequency of interest is required for accurate capture of the PCs. Shape variations resulting from shaft vibration amplitudes of as small as 0.036 pixels could be detected using the shape analysis approach. Some non-contact vibration measurement techniques such as laser vibrometry may not be ideal for investigating large amplitude vibrations on rotating machinery due to cross coupling effects on the measurements. An increase in vibration amplitudes mean that shape variations are easily noticeable, making this analysis technique even more suitable for those type of cases.

The camera spatial resolution also affects the performance of the proposed approach. In applications where the vibrations amplitudes are in the subpixel range of the camera used to capture the images, variations in the shape of interest may not be captured accurately depending on the form of the shape. This will be the case in those situations where the shape boundary either runs along pixels in the same row or column. In the case of boundaries that traverse pixels in different rows and columns, a high resolution camera will be able to capture a smoother shape boundary, implying that it will be able to capture the shape changes more accurately. To investigate the effect camera resolution has on the quality of results, contours from images of a 1200 rpm rotating Bently Nevada rotor system given in Fig. 2, captured at 420 Frames Per Second (FPS) using a GOM 4 M camera system, were used. These contours were quantized using different bins to replicate how they would appear if they were captured using cameras of different resolutions. Fig. 9 illustrates the appearance of contours quantized with different number of bins for one of the images captured.

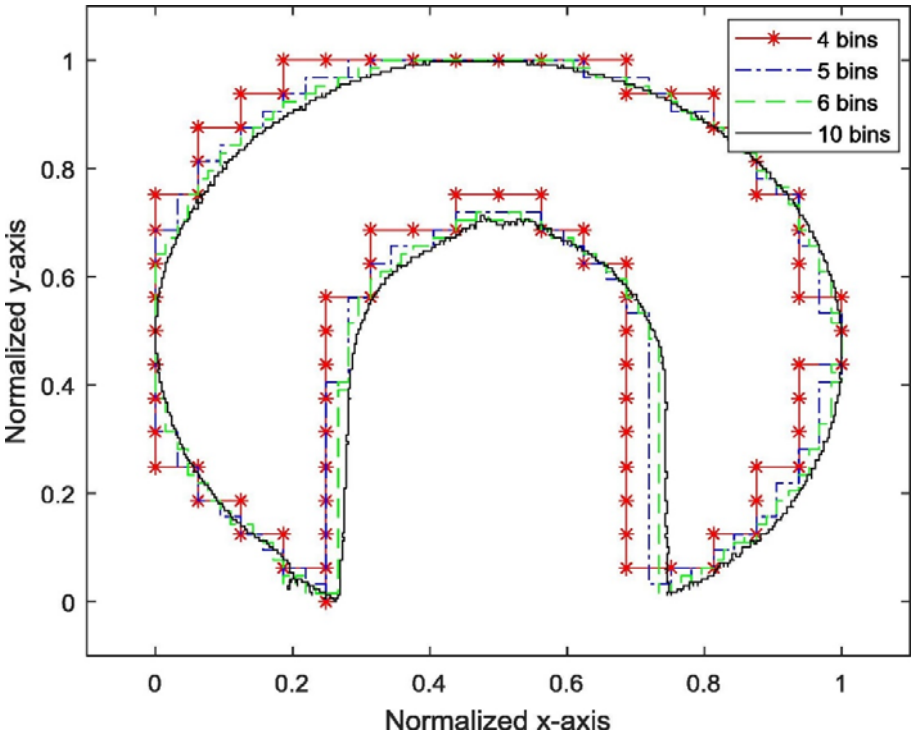

Fig. 9. Differently quantized shape contours.

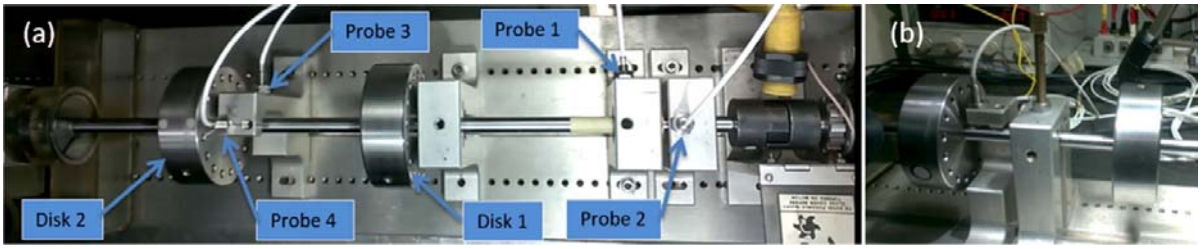

Fig. 10. (a) Positioning of proximity probes, (b) rotor-stator rub application.

The Signal-to-Noise Ratio (SNR) values of PCs time measurements calculated for 6–10 bins were determined. The results obtained are given in Table 1. The SNR was determined as the ratio of RMS energy of the fundamental tone to the RMS of the noise in the signals.

Table 1. Effect of number of quantization bins on the SNR of PCs.

Number of bins	SNR PC 1	SNR PC 2	SNR PC 3	SNR PC 4
6	0.037	0.119	0.132	2.811
7	0.034	0.131	0.152	3.101
8	0.060	0.221	0.273	2.035
9	0.099	0.305	0.411	2.901
10	0.118	0.320	0.419	1.876

As can be noted, there is an expected general increase in the quality of the captured PCs with increasing camera resolution owing to the robustness of shape variation detection when smooth boundaries are being extracted. The form of the shape, how it varies due to a system response and the shape variation associated with each PC (Fig. 4), also contribute to how the resolution affects the quality of the PCs. In the case of PC 4, the resolution does not seem to have a predictable effect on the high SNR. This means that a course shape boundary sometimes aids the sensitivity of PC 4 shape variation detection, owing to the form of shape variation associated with it (four lobed, Fig. 4), and the way the shaft vibrates in this case. In general however, a higher resolution will always be favourable when capturing small vibration responses associated with small extracted shapes.

5. Experimental dynamic analysis of the rotor system

A GOM 4 M stereo videography system was used to capture images of the rotor at 420 FPS. The system was balanced at a rotational speed of 1200 rpm. Six investigations were conducted to capture variations in PCs resulting from different machine faults. These faults include rotor unbalance, hydrodynamic bearing oil instabilities and rotor-stator rub. As reference, Meggitt proximity transducers with sensitivities of 8 V/mm and measuring ranges of 2 mm were employed. These were located at positions indicated in Fig. 9(a). Rotor unbalances were introduced at disk 1 and disk 2, and shaft rub condition applied at the mid-point of the two disks by screwing a bronze stud onto the shaft (Fig. 9(b)).

The four different unbalance cases investigated are given in Table 2.

Table 2. Unbalance cases.

Case	Unbalance on Disk 1	Unbalance on Disk 2	Unbalance Type
1	5.62 g at 0^0	0	static
2	0	5.62 g at 0^0	static
3	4.85 g at 0^0	4.85 g at 0^0	couple
4	4.85 g at 0^0	4.85 g at 180^0	couple

5.1. Rotor dynamic behaviour investigation using orbit plots

Time domain measurements from the proximity transducers were analysed first to get general idea of how the system was behaving. Orbit plots from probe 3 and 4 measurements (Fig. 11) indicate differences in the shaft whirling vibrations for the different operating conditions. It is these differences in vibrations that have to be detected and distinguished using shape analysis for condition monitoring purposes.

The shaft whirling motion for the cases with unbalance can be recognized from the close to circular orbit plots. Oil instabilities result in a tilted elliptical orbit. The shaft is prevented from motion in the upward direction in the rotor-stator rub investigation, which can be clearly noticed from the flat-topped orbit plot.

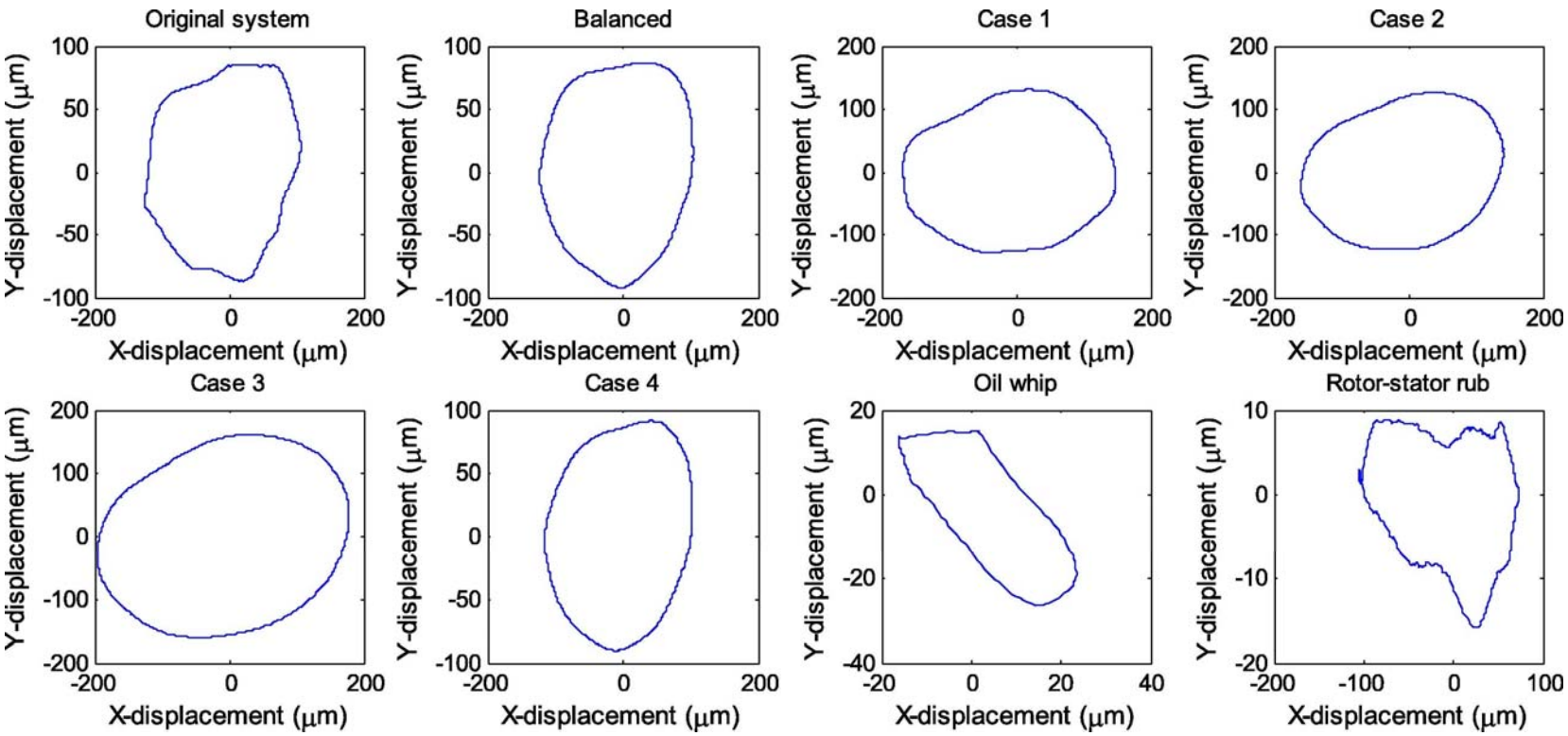

Fig. 11. Orbit plots for probes 3 and 4.

5.2. Rotor unbalance investigation

System rotor unbalance was investigated in detail, with conventional measurement results from proximity probes being analysed first. How well these measurements can distinguish between the different operating conditions was investigated, and then compared to how well shape based PCA performs.

Frequency domain proximity sensor measurements are given in Fig. 12, Fig. 13. Probes 1 and 2 are located at the bush bearing supported end of the shaft, where the shaft vibrations are more restricted compared to those at the hydrodynamic bearing end (probes 3 and 4). Due to that interference, the low SNR of the measurements from probe 1 and 2 results in the more significant sub-harmonic frequency components observed in Fig. 12, Fig. 13.

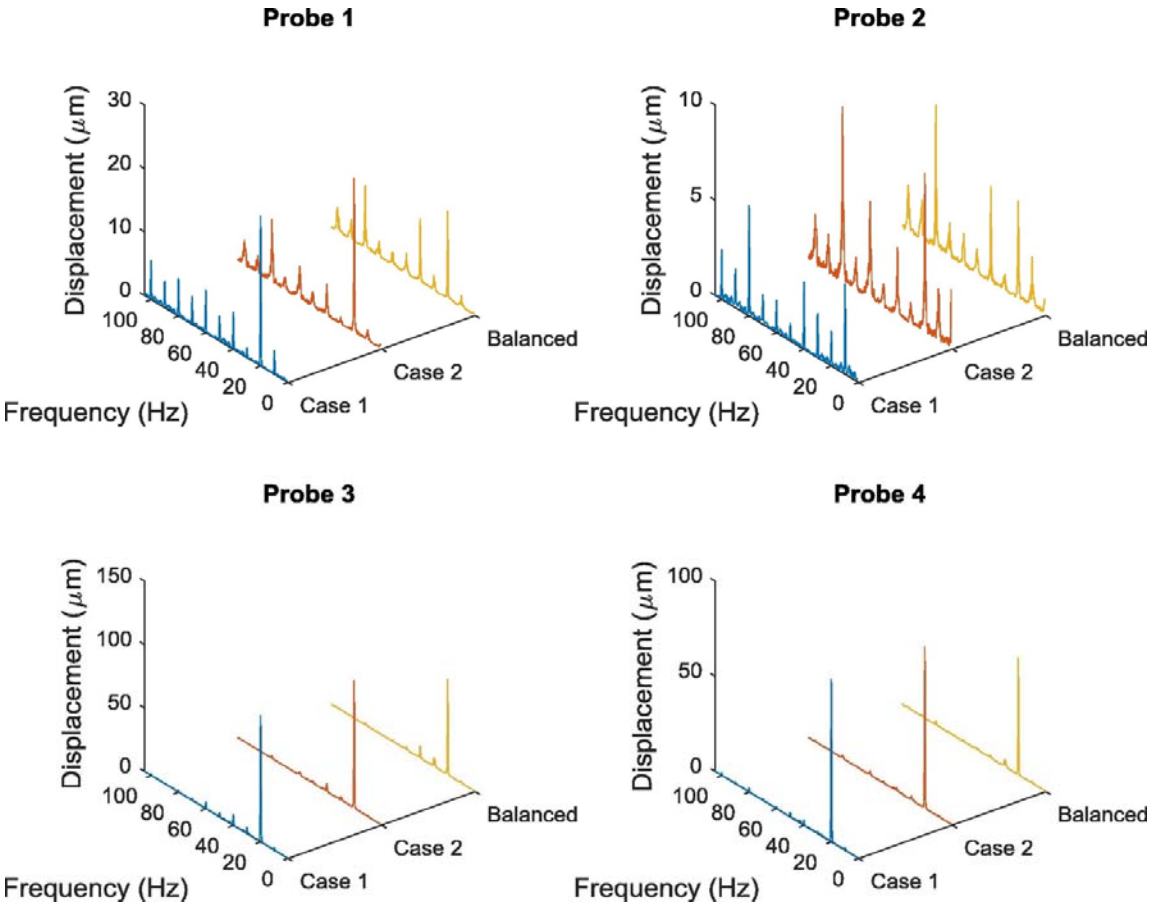

Fig. 12. Proximity probes based static unbalance.

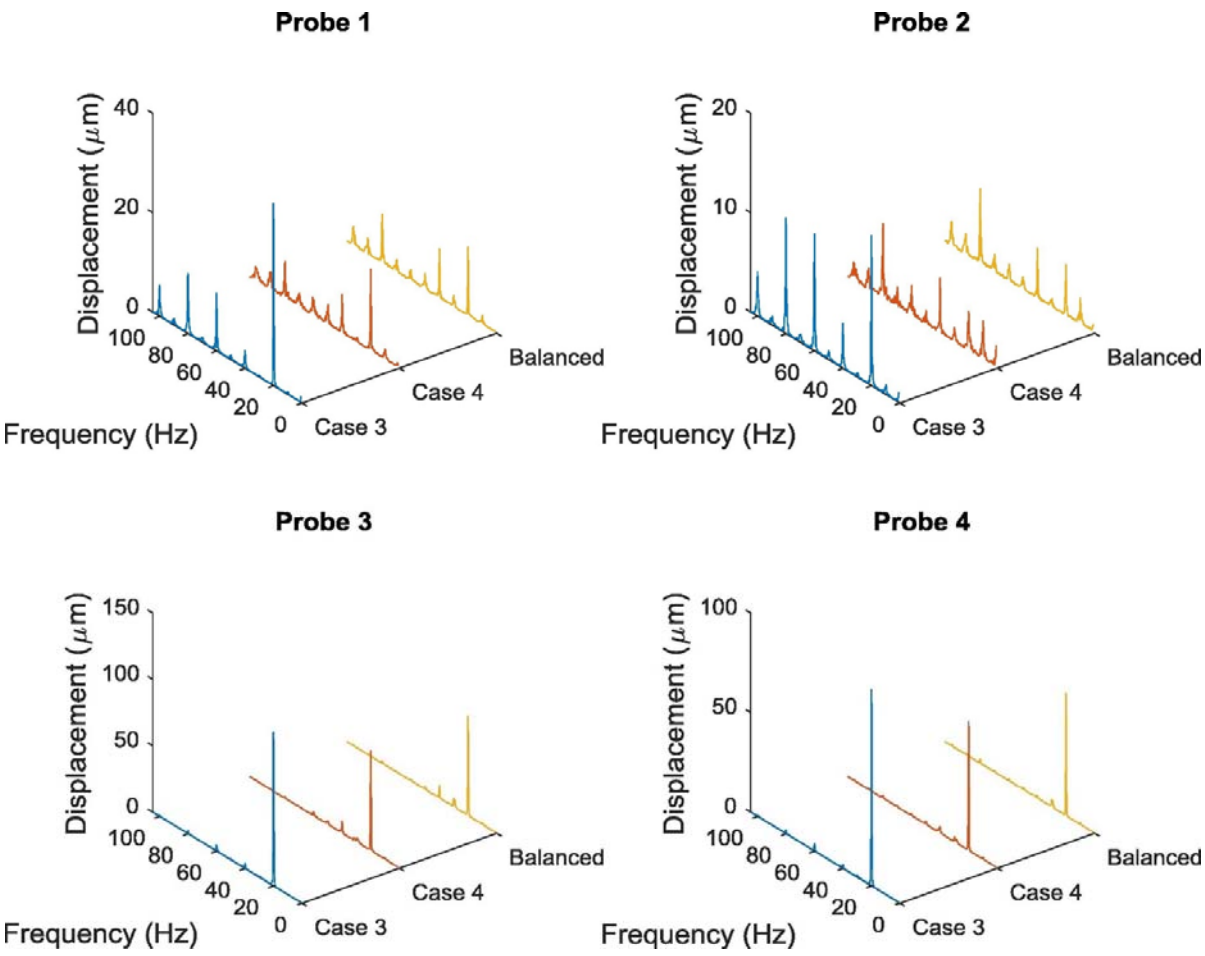

Fig. 13. Proximity probes based couple unbalance.

Focusing on probes 3 and 4, a frequency domain proximity sensor measurement analysis does not yield significant information in terms of classification of system unbalance. This is illustrated in Fig. 12, Fig. 13. Whilst the introduction of unbalance clearly results in a general increase of fundamental frequency magnitudes for the probes, variations between different static and couple unbalance operating conditions are not apparent.

The conventional phase analysis approach, which involve determining the fundamental frequency phase differences between various probes, was employed to detect, classify and distinguish the different forms of unbalance using measurements from the proximity probes. A value of 90° (±30° to account for mechanical variance, according to [19]) between the vertical and horizontal probes at any particular bearing indicates the presence of unbalance. This is expected regardless of the type of unbalance present in the system. Distinguishing unbalances entails the analysis of phase measurements for probes measuring in the same direction but at different bearings. For a statically unbalanced system, a phase difference of 0° (±30°) is expected. This phase difference will be approximately 180° for a couple unbalanced system. Dynamic unbalance, which is a combination of both static and uncouple unbalance, can be identified by a phase difference between 0° and 180°.

Shown in Table 3 are the phase analysis results. Probes 1 and3 were measuring the horizontal shaft position at different bearings, and probes2 and 4 the vertical shaft position (refer to Fig. 10).

Table 3. Proximity probes phase analysis.

System state	Phase difference (Probes 1 and 2)	Phase difference (Probes 3 and 4)	Phase difference (Probes 1 and 3)	Phase difference (Probes 2 and 4)
Balanced	289.6°	275°	12.8°	1.8°
Case 1	180.7°	273.2°	0.3°	92°
Case 2	89.6°	80.6°	8.5°	0.5°
Case 3	174.5°	82.9°	2.6°	89°
Case 4	46.3°	85.2°	2.6°	134°

Considering signals from proximity probes 3 and 4, Table 3 indicates the presence of unbalance in the system, with the exception of Case 1 (static unbalance at disk 1). The effect of unbalance at disk 1 is not apparent enough in these results. Probes 1 and 2 only indicate the presence of unbalance for Case 2, something that can be attributed to the probes being located quite close to the journal bearing. Shaft vibration amplitudes are very low, and the SNR is also low. Analysing phase values for probes at different bearings, Table 3 indicates the presence of dynamic unbalance in the system for all the cases investigated. This was expected as some form of residual unbalance always remains after a system has been balanced, with the unbalance effect being more significant for small systems.

An investigation using shape analyses was then employed to check if the different system operating conditions could be better distinguished. For the Bently Nevada rotor system, this could not be conclusively done using data from the proximity probes.

Fig. 14 shows the PC results obtained for static unbalance. It should be noted that PC results from captured images tend to have a significant noise floor. The roughness of the extracted shape at the local boundary pixels varies from image to image.

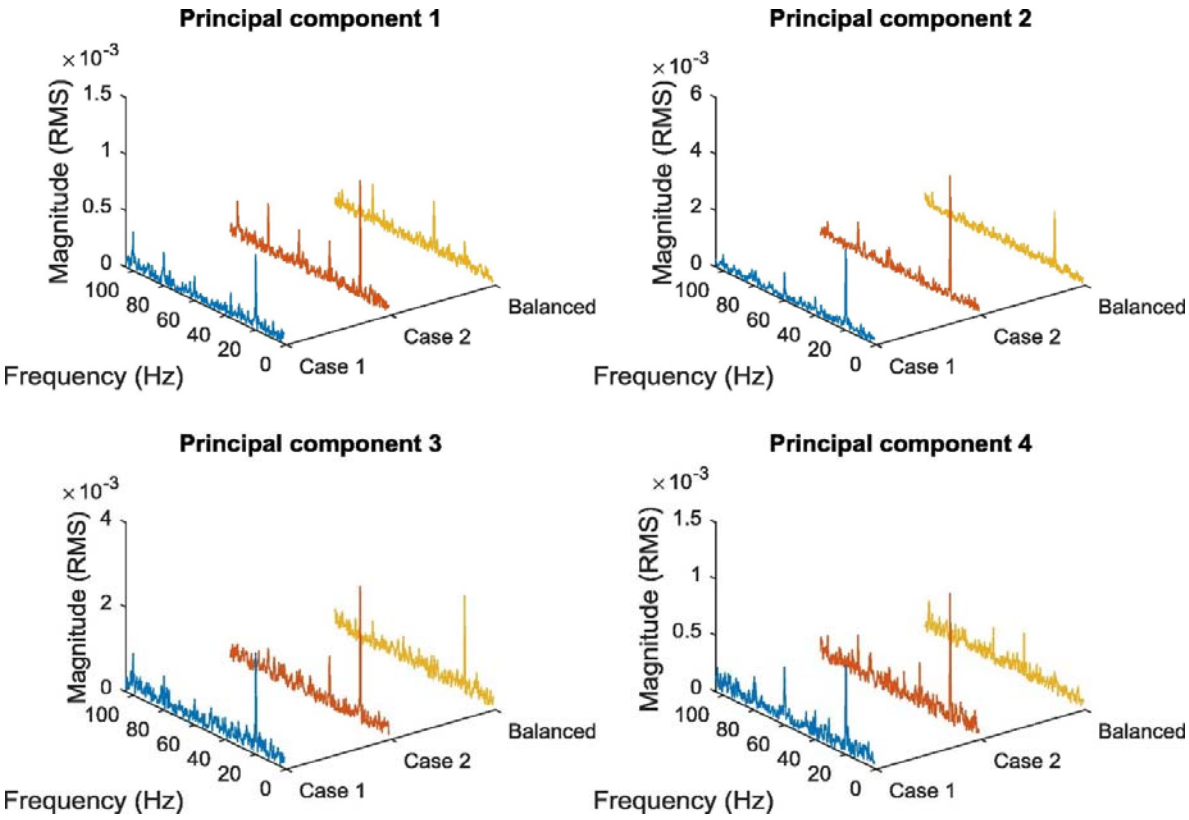

Fig. 14. Principal component based frequency responses for static unbalance.

Application of static unbalance at either disk 1 or disk 2 increases the forced rotor whirling motion, thus resulting in more significant shape variations. This is evident from the increased PC magnitudes observed in Fig. 14. The additional unbalancing masses added produces larger shape variations compared to the ones resulting from the residual unbalance in a 'balanced' system. Case 2 involves addition of unbalance on disk 2, which is located closer to the shaft central location and furthest from the two bearing supports. It is expected that the energy introduced to the system in Case 2 be greater than that introduced in Case 1. This is evident from the PC magnitude differences in Fig. 14.

Static unbalance results in a very different frequency structure for PCs measurements (comparing Fig. 12, Fig. 13, Fig. 14). Energy introduced into the system by a static unbalance results in a shape variation that is predominantly associated with the rotational speed. This difference between a balanced and the two statically unbalanced system cases is not that apparent when considering probe based measurements (Fig. 12). This is illustrated in Table 4. The harmonic Magnitude Increase Factors (MIFs) for each case are calculated relative to the balanced system values using Eq. (5). A zero value indicates the absence of a peak at a particular harmonic for the unbalance case of interest. A '-' indicates absence of a peak for the balanced system, and a peak present for the unbalance case.

$$MIF = \frac{Unbalance\ \ system\ \ magnitude - Balanced\ \ system\ \ magnitude}{Balanced\ \ \ system\ \ magnitude} \qquad (5)$$

Table 4. Harmonic magnitude increase factors for static unbalance.

	1× harmonic MIF		2× harmonic MIF		3× harmonic MIF	
	Case 1	**Case 2**	**Case 1**	**Case 2**	**Case 1**	**Case 2**
PC 1	1.62	3.18	0	−0.18	–	–
PC 2	0.37	1.13	–	–	–	–
PC 3	0.02	0.39	0	–	0	0
PC4	–	–	0	0.01	0.54	0
Probe 4	0.39	0.38	0	0	0	0

The first harmonic PCs MIFs from Table 4 clearly indicate an increase in the system response magnitudes as a result of the static unbalance. Case 2 MIFs for the PCs are significantly higher than those for case 1 as expected, making a distinction between the two unbalance cases possible. This can be adopted for quantifying the extent of static unbalance in a system. Measurements from the proximity probes do not capture the differences in static unbalance for this case. For static unbalance, MIFs at the higher harmonics do not yield significant fault classification information except for PC 2. Higher harmonics are noticed in the system the moment static unbalance is introduced.

Fig. 15. shows the PC results obtained after introducing couple unbalance into the system (Case 3 and 4).

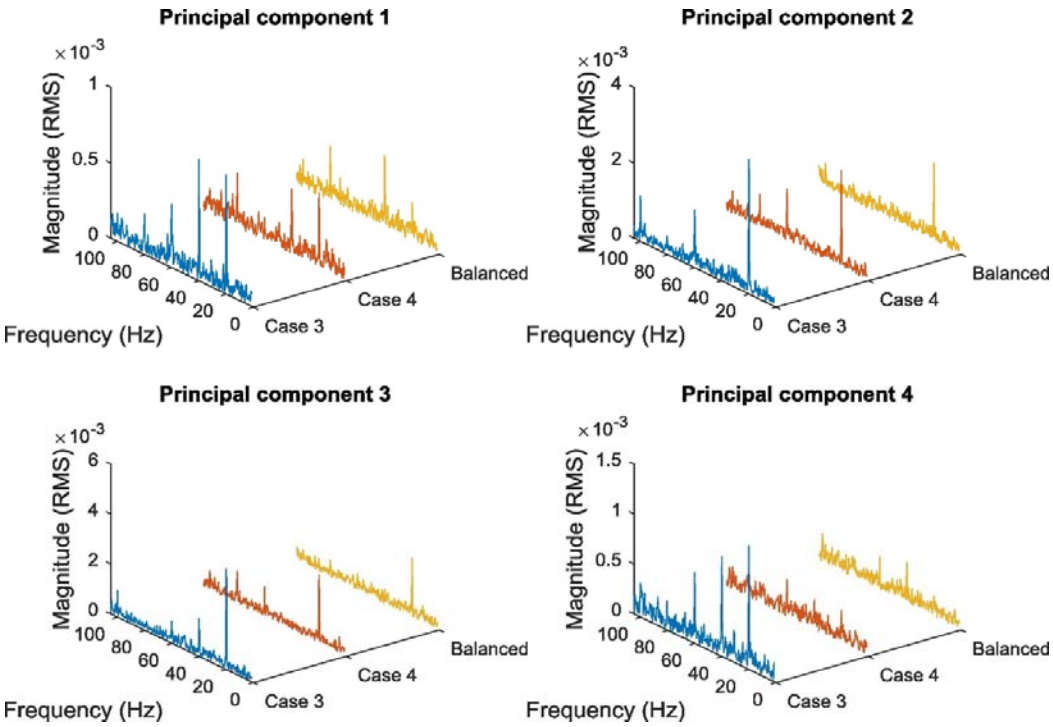

Fig. 15. Principal component based frequency responses for couple unbalance.

Comparing Fig. 14, Fig. 15, it can be clearly noted that there are significant differences in shape variations introduced by the presence of either static or couple unbalance in the system (PC 1 and PC 4). Static unbalance imposes rotor whirling that results in a bent Operational Deflection Shape (ODS) around the shaft reference axis. The ODS has a form similar to the first bending mode. This results in a general increase in the magnitude of the fundamental frequency component for all the PCs, when analysed relative to a balanced system with some residual unbalance in it. On the other hand, depending on the positioning of the unbalance weights, the ODS associated with couple unbalance can be more complex taking forms similar to how the shaft higher bending modes would appear. Thus, the shaft whirling motion will result in complex shape variations, which do not correlate directly with the basic PC shape variations, resulting in the higher harmonics receiving even more energy in a frequency domain analysis. This explains the higher frequency component magnitudes at 40 Hz for PCs 1 and 4. This can be used to differentiate between static and couple unbalance in a system.

To illustrate this further, Table 5 shows the MIFs determined for the rotor system. Couple unbalance introduced at the same angle on different shaft locations (case 3) clearly results in increased system energy as indicated by the higher case 3 first harmonic MIFs. Comparing Table 4 results to Table 5, PCs 1 and 4 s harmonic MIFs indicate a difference between static and couple unbalance. Couple unbalance clearly results in a significant increase (case 3) or significant decrease (case 4) of the second harmonic PCs magnitudes. This is not the case with static unbalance. In addition all PCs show an increase in the third harmonic magnitudes in the presence of couple unbalance.

Table 5. Harmonic magnitude increase factors for couple unbalance.

	1× harmonic MIF		**2× harmonic MIF**		**3× harmonic MIF**	
	Case 3	**Case 4**	**Case 3**	**Case 4**	**Case 3**	**Case 4**
PC 1	2.12	0.96	0.69	−0.99	–	–
PC 2	0.73	0.24	0	0	–	–
PC 3	0.71	0.16	–	0	–	–
PC4	–	–	1.42	−0.27	1.12	0.10
Probe 4	0.6	0.05	0	0	0	0

Comparing the proximity probe measurements (both phase analysis and single probe frequency domain measurements) to shape PCA in terms of unbalance investigations, it is evident that proposed shape analysis approach offers results that easily illustrate different system operating conditions. Variations in system dynamics that are too small to be clearly captured using uniaxial transducers are much more easily identified by using the 2D based data capturing scheme.

5.3. Rotor-stator rub investigation

The superior sensitivity of 2D based analysis in detecting system operating changes was also illustrated in the case of rotor-stator rub. Fig. 16 indicates that rotor-stator rub results in a decrease in fundamental frequency magnitude for the proximity probes. This is expected since the amplitude of vibration response in a particular direction is reduced if a component is interfering with the shaft in that direction. Advanced probes to capture signals with high SNRs might need to be employed to diagnose a system operating in these conditions. This is however different when considering PCs. The 2D analysis approach focuses on the variation of an initial shape, an occurrence which can be amplified by the presence of rotor-stator rub. This is evident in PCs 1, 2 and 4 of Fig. 17. In this case the decrease in the magnitudes of individual axis responses did not decrease the quality of the measurements captured. Changes in the overall behaviour of a system here were better captured using a multi-dimensional approach such as the proposed shape analysis.

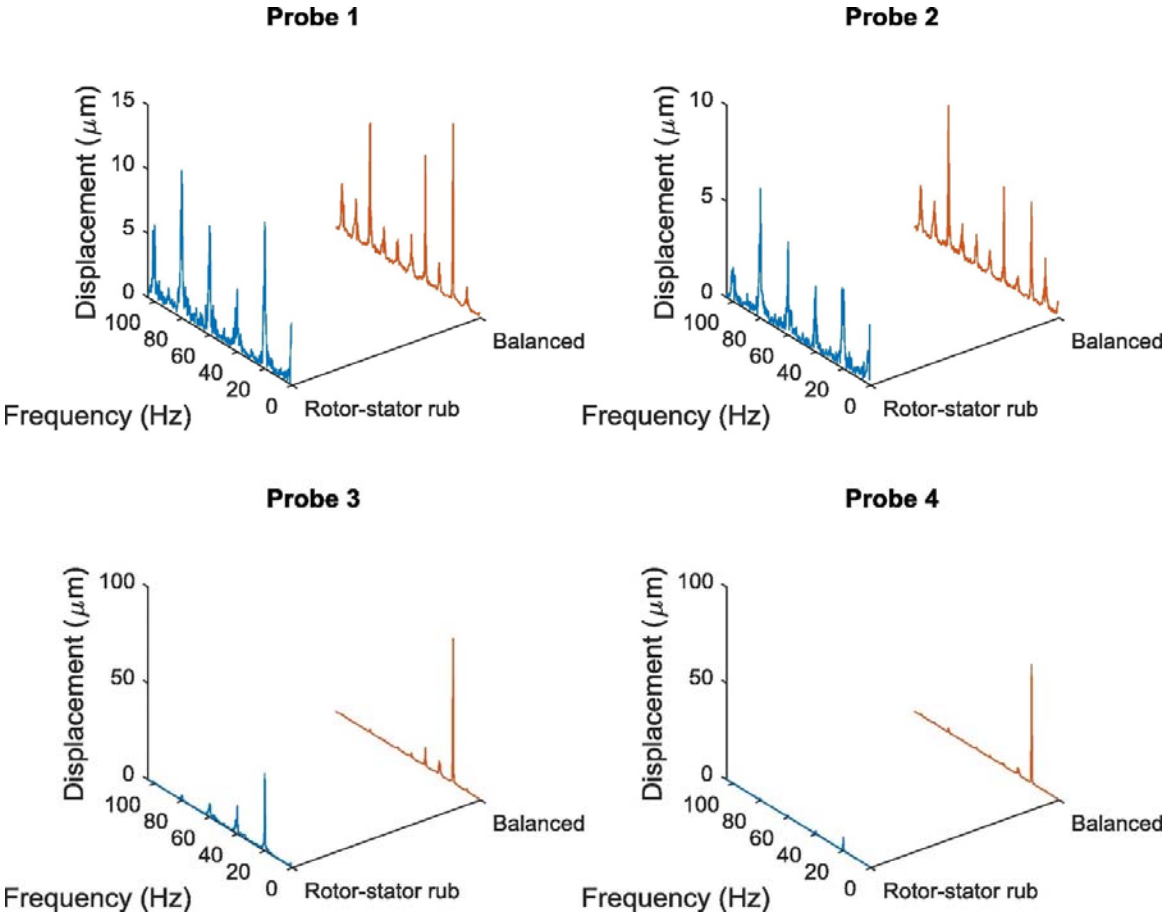

Fig. 16. Proximity probes rotor-stator rub.

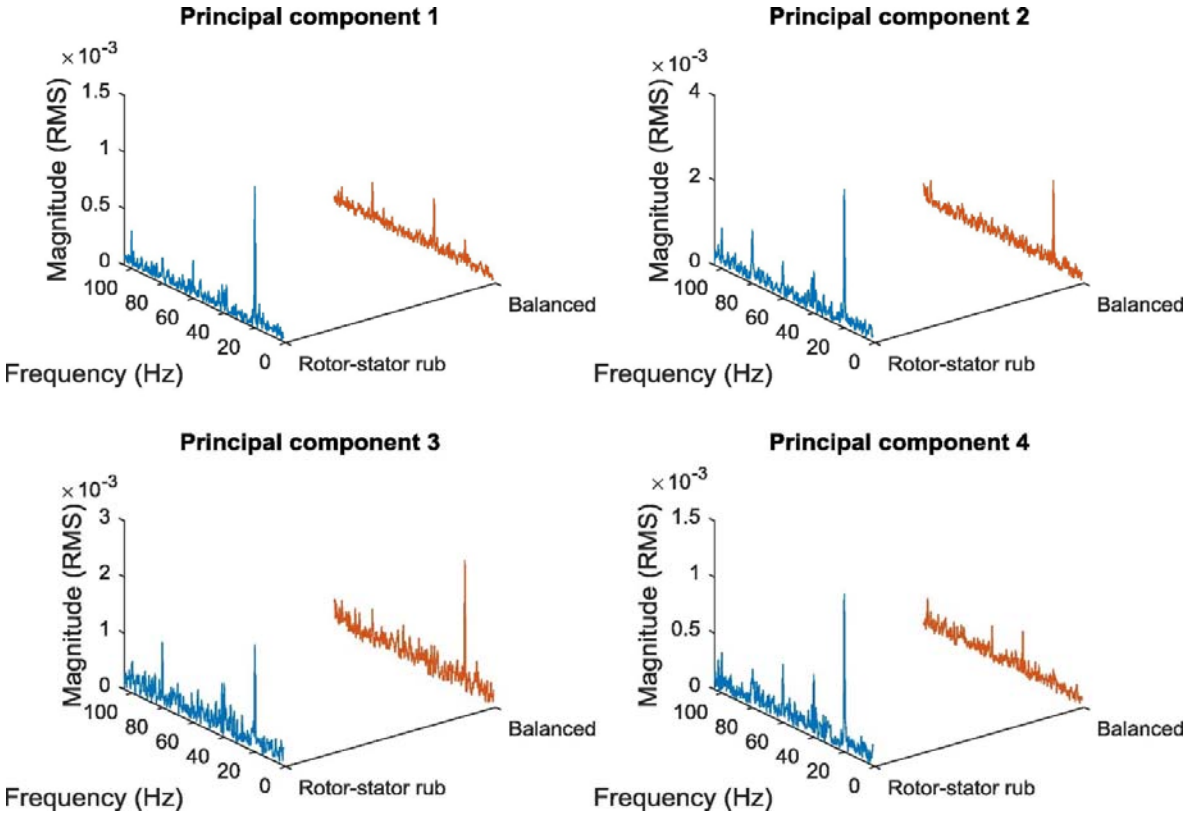

Fig. 17. Principal component based frequency responses for rotor-stator rub.

5.4. Hydrodynamic bearing oil instabilities investigation

Hydrodynamic bearing oil instabilities tend to be one of the most dangerous faults in rotating machines owing to the fact that system failure of a structure exhibiting oil whip characteristics occurs in a very short period of time. Therefore hydrodynamic bearing oil instabilities were also investigated to check if the proposed approach can capture information that can allow for easier identification of bearing oil instabilities.

When a rotor system is running at a particular speed, the fluid flows around the bearing at a speed that is approximately half the journal surface speed. This will then introduce oil whirl motion into the system, of which the sub-synchronous frequency will be slightly less than 50% of the shaft rotational frequency. If the shaft rotational speed is then set to twice the first critical speed, then the oil whirl motion will then coincide with the critical speed. Energy from the oil whirl instability will now be exciting the first bending mode resulting in a system instability. The vibratory responses associated with the instability often cause failure in a short period of time [20]. To experimentally determine the rotor system critical speeds, a system run up and run down was conducted, and the in-plane shaft positions from proximity probes 3 and 4 extracted. Increased shaft vibrations are expected when the rotor spin speed coincides with a critical speed. The speed was increased from about 175 rpm to 5420 rpm.

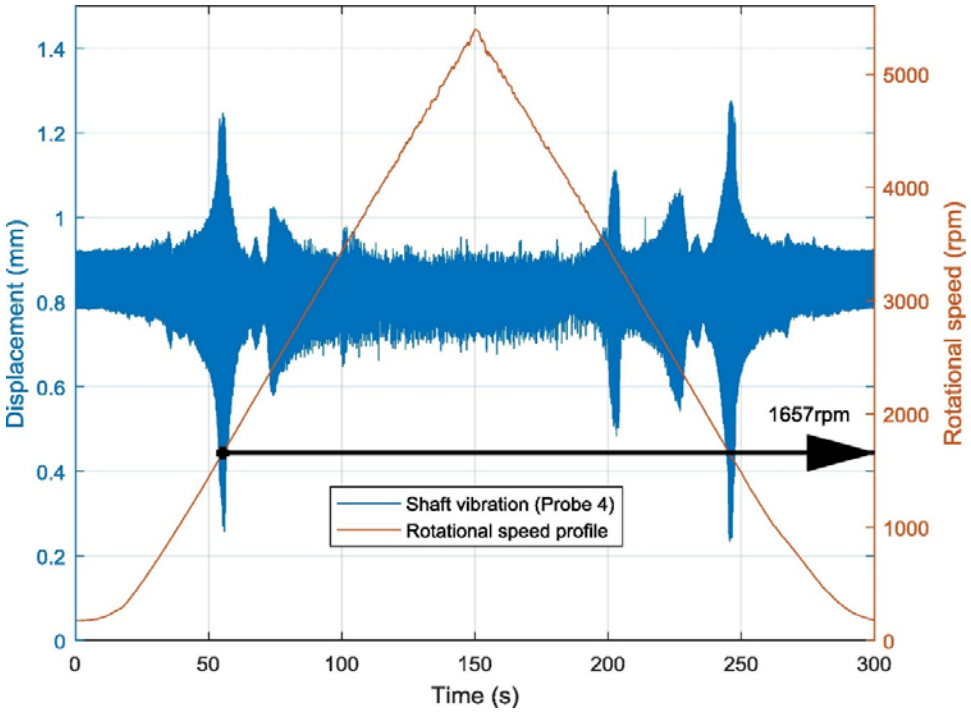

Fig. 18. Rotational speed ramp up and down system response.

From Fig. 18 it can be noted that the first critical speed of the system is 1657 rpm. Thus setting a rotational speed to 3314 rpm, which is twice the critical speed, will induce oil whirl. Fig. 19 shows the responses obtained from the proximity probes when the system rotational speed is set to 3314 rpm. Except for probe 2, the probes reflect the highest vibratory frequency magnitudes to be located at the shaft critical speed, with significant peaks at the system rotational speed as well.

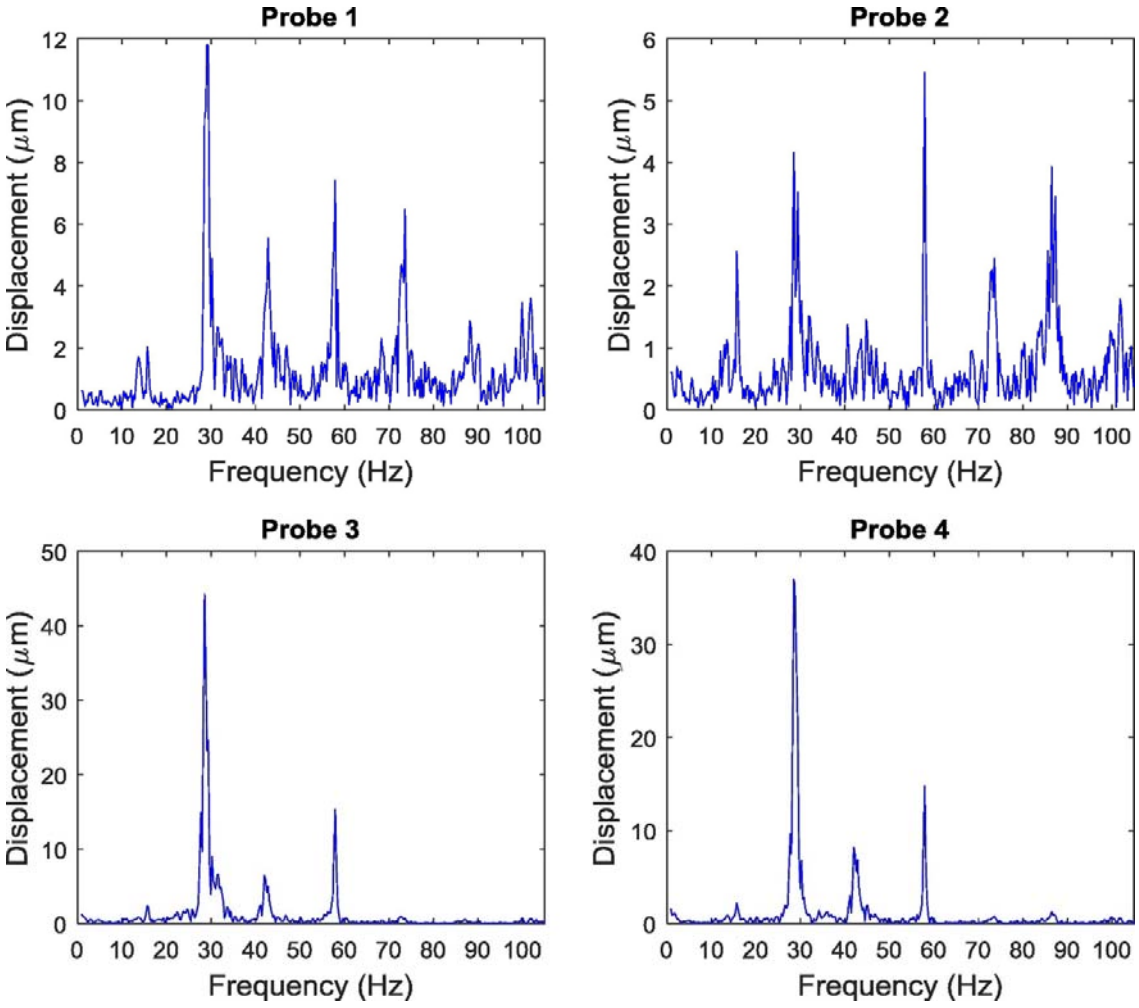

Fig. 19. Proximity probes oil instability effects.

A different behaviour is however observed for the PCs, as shown by Fig. 20.

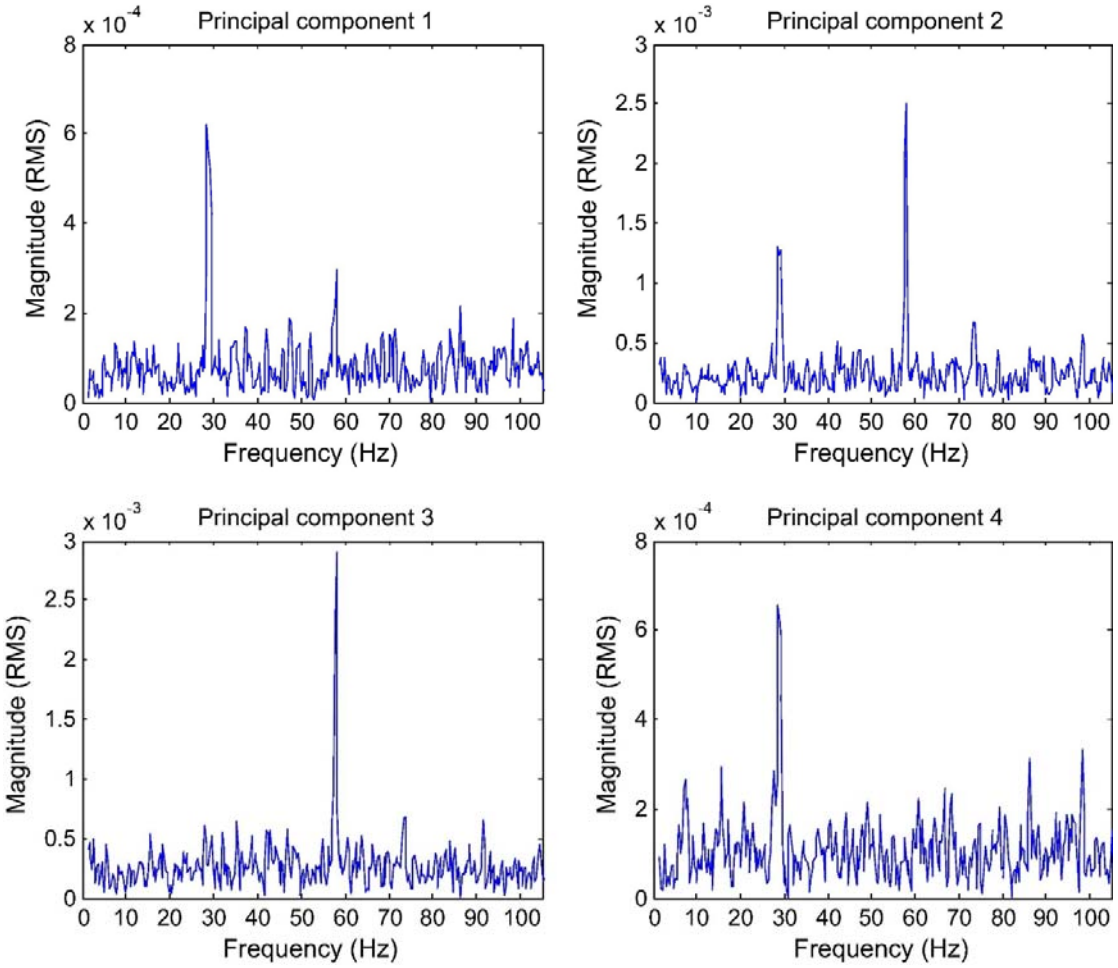

Fig. 20. Principal components based oil instability effects.

Hydrodynamic bearing oil instabilities consists of multiple events (rotating shaft and oil whirl effect) contributing to the overall system behaviour. Measurements from a proximity probe will be composed of all this information. On the other hand, a shape PCA based investigation implies that the four PCs determined from an image captured using a single camera are uncorrelated with each other.

Whilst PCs 1 and 4 clearly show peaks at the shaft critical speed, PCs 2 and 3 show peaks at the system rotational speed. This indicates that the system dynamics introduced by oil instabilities have less influence on shape variations associated with PCs 2 and 3 as compared to the effect general shaft whirling due a particular rotational speed has. These distinct differences in the form of the four PCs analysed for the same system condition are noticed only for a system where oil instabilities are present. Thus the variability in the parameters captured using a single sensor in 2D shape analysis offers more tools that can be monitored separately to fully understand the dynamics of a rotating machine.

6. Conclusion

A 2D shape analysis approach for condition monitoring of rotating machines is proposed. The proposed approach was applied to a modified Bently Nevada rotor system to investigate whether different system faults could be isolated. The shape of interest in the current investigation was chosen to be at the bearing housing, with the aim of verifying system dynamics using proximity probes attached there.

System unbalance, rotor-stator rub and hydrodynamic bearing oil instabilities all resulted in shape based PC variations different from each other, allowing isolation of various system faults. These observations illustrated the applicability of this data acquisition and analysis strategy as an optical targetless non-contact vibration based condition monitoring tool. The obtained results were also evaluated to allow the approach to be used not only for detecting different system behaviours, but also to classify different faults in the system. Different levels of static unbalance, in terms of the size of the unbalancing mass, were differentiated in terms of how much the shape of interest changed. Higher harmonics in the spectral analysis data resulting from the shape variations associated with couple unbalance complex shaft ODSs allowed differentiating couple unbalance from static unbalance. For the system considered, this distinction between different forms of system unbalance could not be done conclusively through phase analysis of the conventional proximity probe measurements.

The proposed approach also proved to be valuable when investigating very small vibrations and complicated system responses. From the rotor-stator rub investigation, it could be clearly shown that the multi-dimensional nature of shape analysis allows easier detection of changes in a system even in cases where the uniaxial point vibrations captured by proximity probes are very small. In these cases, conventional contact transducers tend to have very low SNRs, usually complicating accurate fault detection. For a system undergoing hydrodynamic bearing oil instabilities, the uncorrelated nature of the determined PCs illustrated how interlinked responses in a system (rotating shaft and oil whirl effect) can be better isolated for further analysis by looking at different PCs (PC 3 and 4 in this case).

This paper demonstrates the feasibility of the proposed measurement approach for monitoring rotating machines. The approach shows great potential in terms of limiting the number of sensors needed to fully diagnose a turbomachine whilst in operation, through the use of a non-contact and non-intrusive transducer. Being based on shape variations, the proposed approach is capable of capturing high amplitude vibrations of structures, with no prior surface preparations requirements. This makes the approach more favourable to applications were the other non-contact measurement techniques such as DIC and LDV struggle to perform. In applications such as extracted blade contours where the full shape of interest does change, the determined ODSs PCs spectral data coupled with the shape variations associated with each specific PC can be used to better understand the multi-dimensional system dynamic behaviour.

Acknowledgement

This research was funded by the Eskom Power Plant Engineering Institute (EPPEI) South Africa. (Grant number: EP0001).

References

[1] R. Wu, Y. Chen, Y. Pan, Q. Wang, D. Zhang, Determination of three-dimensional movement for rotary blades using digital image correlation, Opt. Lasers Eng. 65(2014) 38–45.

[2] B. LeBlanc, C. Niezrecki, P. Avitabile, J. Chen, J. Sherwood, Damage detection and full surface characterization of a wind turbine blade using three-dimensional digital image correlation, Struct. Heal. Monit. 12 (2013) 430–439.

[3] J. Baqersad, C. Niezrecki, P. Avitabile, Full-field dynamic strain prediction on a wind turbine using displacements of optical targets measured by stereophotogrammetry, Mech. Syst. Signal Process. 62–63 (2015) 284–295.

[4] H.F. Zhou, H.Y. Dou, L.Z. Qin, Y. Chen, Y.Q. Ni, J.M. Ko, A review of full-scale structural testing of wind turbine blades, Renew. Sustain. Energy Rev. 33 (2014) 177–187.

[5] J. Winstroth, L. Schoen, B. Ernst, J.R. Seume, Wind turbine rotor blade monitoring using digital image correlation: a comparison to aeroelastic simulations of a multi-megawatt wind turbine, J. Phys. Conf. Ser. 524 (2014) 12064.

[6] M. Ozbek, D.J. Rixen, O. Erne, G. Sanow, Feasibility of monitoring large wind turbines using photogrammetry, Energy. 35 (2010) 4802–4811.

[7] L.E. Olson, A.I. Abrego, D.A. Barrows, A.W. Burner, Blade deflection measurements of a full-scale UH-60A rotor system, Am. Helicopter Soc. Aeromechanics Spec. Conf. (2010) 738–747.

[8] E. Zappa, P. Mazzoleni, A. Matinmanesh, Evaluation and improvement of digital image correlation uncertainty in dynamic conditions, Opt. Lasers Eng.56 (2014) 140–151.

[9] C.N. Mark, N. Helfrick, P. Pingle, P. Avitabile, Optical Non-contacting Vibration Measurement of Rotating Turbine Blades, in: Imac-Xxviii, Society for Experimental Mechanics Inc., Orlando, Florida USA, 2010, pp. 281–290.

[10] B. Gwashavanhu, A.J. Oberholster, P.S. Heyns, Rotating blade vibration analysis using photogrammetry and tracking laser Doppler vibrometry, Mech. Syst. Signal Process. 76–77 (2015) 174–186.

[11] C. Warren, C. Niezrecki, P. Avitabile, Optical Non-contacting Vibration Measurement of Rotating Turbine Blades II, in: IMAC-XXVIII, 2010, pp. 39–44.

[12] I.K. Kazmi, L. You, J.J. Zhang, A survey of 2D and 3D shape descriptors, 2013 10th Int. Conf. Comput. Graph. Imaging Vis. 2013 (2013) 1–10.

[13] H.K. Mebatsion, J. Paliwal, D.S. Jayas, Evaluation of variations in the shape of grain types using principal components analysis of the elliptic Fourier descriptors, Comput. Electron. Agric. 80 (2012) 63–70.

[14] D. Zhang, G. Lu, Review of shape representation and description techniques, Pattern Recognit. 37 (2004) 1–19.

[15] H. Freeman, Computer processing of line-drawing images, Comput. Surv. 6 (1974) 58–97.

[16] N.A. Jusoh, J.M. Zain, Application of freeman chain codes: an alternative recognition technique for Malaysian car plates, Int. J. Comput. Sci. Netw. Secur.9 (2009) 222–227.

[17] F.P. Kuhl, C.R. Giardina, Elliptic Fourier features of a closed contour, Comput. Graph Image Process (1982).

[18] B. Gwashavanhu, P.S. Heyns, A.J. Oberholster, Statistical shape analysis as anon-contact method for condition monitoring of turbomachines – sensitivity analysis, in: J.K. Sinha (Ed.), Proc. 2nd Int. Conf. Maint. Eng., Manchester, 2017.

[19] SKF Reliability Systems: Vibration Diagnostic Guide CM5003, (n.d.). http://edge.rit.edu/edge/P14453/public/Research/SKF VibrationGuide.pdf (accessed January 9, 2018).

[20] F.C. Nelson, Rotor Dynamics without Equations, Int. J. COMADEM. 10 (2007) 2–10.